# Microstructural insights into the coercivity enhancement of grain-boundary-diffusion-processed Tb-treated Nd–Fe–B sintered magnets beyond the core-shell formation mechanism

K. Žagar Soderžnik[a], K. Žužek Rožman[a,g], M. Komelj[a], A. Kovács[b], P. Diehle[b], T. Denneulin[b], A. Savenko[c], M. Soderžnik[d], S. Kobe[a,g], R. E. Dunin-Borkowski[b], J. Mayer[b,e], B. Markoli[f], S. Šturm[a,g]

[a]*Department for Nanostructured Materials, Jožef Stefan Institute, Ljubljana, SI-1000, Slovenia*

[b]*Ernst Ruska-Centre for Microscopy and Spectroscopy with Electrons and Peter Grünberg Institute, Forschungszentrum Jülich, 52425 Jülich, Germany*

[c]*Central Institute for Engineering, Electronics and Analitics, ZEA-3: Analytics, Forschungszentrum Jülich, 52425 Jülich, Germany*

[d]*Laboratory for Tribology and Interface Nanotechnology (TINT), Faculty for Mechanical Engineering, University of Ljubljana, Ljubljana, SI-1000, Slovenia*

[e]*RWTH Aachen, (Aachen), Germany*

[f]*Department of Materials and Metallurgy, Faculty of Natural Sciences and Engineering, University of Ljubljana, 1000 Ljubljana, SI-1000, Slovenia*

[g]*International Postgraduation School of Jozef Stefan, Ljubljana, SI-1000, Slovenia*

## Abstract

We propose a dominant core-shell formation mechanism for grain-boundary-diffusion-processed (GBDP), Tb-treated, Nd-Fe-B sintered magnets. A Tb-treated Nd-Fe-B magnet was examined from the Tb-oxide-deposited surface into the central part of the magnet, where the increase in coercivity was 30 % compared to a non GBDP Nd-Fe-B magnet. A structure-chemistry-magnetic-property analysis revealed the dominant GBDP mechanism. On the surface of the Tb-treated magnet the Tb is released from the starting precursor following a

cascade of chemical reactions between the Tb oxide and the Nd and/or Nd-Fe-B. The released Tb diffuses along the grain boundaries and the core-shell structures are formed, mainly involving a solid-state diffusion mechanism. The calculated optimum concentration for a 30 % increase in coercivity was 50 ppm of Tb. Off-axis electron-holography measurements indicated 26 % more magnetic induction in the core than the shell, which has a lower magnetic saturation because it contains Tb. The domain-wall width was measured from magnetic phase maps, and gave a good quantitative match with the calculated values. The study showed that the increase in the coercivity is due to a structural effect, and not the magnetic contribution of the Tb. This paves the way towards grain-boundary-engineering studies that will increase the coercivity of Nd-Fe-B magnets for e-mobility and eco-power applications.

## 1. Introduction

The transition to a low-carbon society and energy efficiency by 2050 ("the EUs Green Deal") [1] will require radical solutions to reduce greenhouse-gas emissions by 80 %. The major contributing segments are the development of e-mobility and the generation of eco-power. As part of the EU's green policies, the internal combustion engines that power vehicles will be replaced by electric motors. Sales of such vehicles are expected to exceed those of gasoline and diesel vehicles by 2040 [2]. Even by the end of 2020 there should already be 10 million electric vehicles (EVs) on the road, up from just 1 million in 2015, with the number is expected to reach 150 million EVs by 2050 [2]. Volkswagen have stated that the strategic target of 1 million electric cars will be reached by the end of 2023, two years earlier than previously predicted [3]. However, this transition is only possible with the use of high-performance permanent magnets

(PMs) based on rare earths (REs) and transition metals (TMs) as the key components in highly efficient traction motors and generators for electric, fuel-cell, hybrid and plug-in hybrid vehicles as well as in efficient wind turbines. From this perspective RE-TM PMs are an important subject of research, with the aim being improved properties in the temperature range up to 200 °C.

A PM's performance can be described by its maximum energy product ($BH_{max}$). The value of $BH_{max}$ has increased over time, and today's strongest PMs, like Nd-Fe-B, can reach values as high as 474 kJ/m$^3$ at room temperature [4]. Nd-Fe-B magnets dominate the market for RE-TM PMs (>95 % of the market volume) because of their combination of price and performance.

The mechanism of coercivity ($H_{ci}$) in sintered Nd-Fe-B PMs has long been recognized as being due to the magnetic isolation of the individual $Nd_2Fe_{14}B$ grains, based on a Nd-rich grain-boundary (GB) phase surrounding the grains [5]. However, in 2012 the group from NIMS in Tsukuba, Japan, proposed a mechanism based on domain-wall pinning, as they discovered a lot of Fe in the GB phase, and postulated that the phase is ferromagnetic [6]. To date, the findings in the literature remain controversial. The original coercivity mechanism predicts that the nucleation of reverse magnetic domains occurs in regions with a locally low anisotropy, i.e., close to defects or in an area adjacent to non-ferromagnetic grains with higher stray fields. The highest coercivity measured for sintered Nd-Fe-B magnets is ∼900–1500 kA/m, i.e., 1.2–1.9 T [7], which is ∼20–30 % of the anisotropy field of the $Nd_2Fe_{14}B$ phase ($\mu_0 H_A$ ∼5570 kA/m) [8, 9]. For the high operating temperatures in the traction motors of hybrid and full electric vehicles, reaching approximately 200 °C, a ternary Nd-Fe-B sintered magnet cannot be used due to the negative temperature coefficients of the intrinsic coercivity ($\beta = –0.55$–0.65 %/°C) and remanent magnetization ($M_r$) ($\alpha = –0.12$ %/°C) [10]. In other words, an increase of 10 °C will cause ∼6.5 % loss of coercivity. In order to maintain a sufficiently high coercivity at elevated temperatures, it is necessary to have a room-temperature $H_{ci}$ of at least 2400 kA/m [8]. This is theoretically possible by substituting approximately one-third of the Nd atoms with the

heavy rare earths (HREs) Dy or Tb in order to exploit the higher anisotropy field of the $(Nd,Dy/Tb)_2Fe_{14}B$ phase [9]. But, when substituting Nd with Dy or Tb, the remanent magnetization decreases because of the antiferromagnetic coupling of the Dy and Tb with the Fe [11], causing the maximum room-temperature energy product to fall to 250 kJ/m$^3$ [8]. In order to increase the coercivity without sacrificing too much magnetisation, it is necessary to locally add the Dy and Tb from the metal, $Dy_2O_3$, $Tb_3O_4$, $DyF_3$, or $TbF_4$ using the grain-boundary diffusion process (GBDP) [12-19]. With the GBDP the Dy and/or Tb are added in small amounts (a few wt.%) to the surface of already-sintered Nd-Fe-B magnets, where they are then diffused along the grain boundaries towards the magnet's interior, substituting a part of the Nd in the $Nd_2Fe_{14}B$ phase, so forming the so-called core-shell structure of a shell of $(Dy,Nd)_2Fe_{14}B$ surrounding the core of the $Nd_2Fe_{14}B$ phase. It was shown that by optimizing the Dy-rich surface with GBDP, the coercivity could be increased by 30 % with the addition of only 0.2 wt.% Dy [16, 20]. During the process the elevated temperature triggers the diffusion of the HRE from the surface towards the centre of the magnet along the grain boundaries (GBs), and the HRE-rich shells in the outer parts of $Nd_2Fe_{14}B$ grains are formed based on two possible mechanisms. As proposed by Sepehri-Amin et al. [21], during the GBDP at ~900 °C, a small fraction of the $Nd_2Fe_{14}B$ phase melts due to the ternary eutectic reaction at around ~685 °C [22]. At this temperature, the grain boundaries are actually liquid during the GBDP, which enables the efficient diffusion of HRE into the magnet along the liquid GBs [21]. With this, the overall composition along the tie line (isothermal conditions) above the eutectic temperature is shifting towards HRE and consequently the phase field is shifting towards the liquid phase [22], which is known as chemically induced, liquid-film migration [23]. When the magnet cools, larger amounts of HRE epitaxially solidify from the solid/liquid interface in the form of $(Nd,HRE)_2Fe_{14}B$ onto the existing $Nd_2Fe_{14}B$ solid surfaces. This is presumably driven by the lower formation energy of $Tb_2Fe_{14}B$ when compared to $Nd_2Fe_{14}B$ (-3.486 eV/unit cell) [22].

The formation energy for $Tb_2Fe_{14}B$ is not known, but that for $Dy_2Fe_{14}B$ has been reported. Since the atomic numbers of Tb (A=65) and Dy (A=66) are close, the formation energies for the two compounds should not differ by much. Namely, Dy forms $Dy_2Fe_{14}B$ with a formation energy of -7,721 eV/unit cell, and so it is reasonable to assume that $Tb_2Fe_{14}B$ is more stable than $Nd_2Fe_{14}B$, as Nd has A=60 and shares fewer similarities with either Tb or Dy. This mechanism of HRE shell formation would lead into sharp, i.e., faceted appearance of the core-shell boundaries, but accompanied by a high density of structural defects at the core-shell boundary, i.e., the original solid/liquid interface [22, 24].

In the second core-shell formation mechanism the core-shell boundaries do not originate from an initial solid-liquid interface, but rather as a solid-solid interface in which the HRE-rich shells are formed by the substitutional diffusion of Nd by HRE within the surface regions of the $Nd_2Fe_{14}B$ matrix grains from the HRE-rich GBs [22, 25]. Typically, this core-shell formation mechanism will dominate below the eutectic temperature for the Nd-Fe-B system. As a result, the core-shell interfaces can exhibit a curved shape, but one that is structurally intact, i.e., without the presence of planar defects.

It is worth mentioning that the available amount of HRE-rich liquid phase during the chemically induced, liquid-film migration, as proposed by the first model, does not match the observed amounts of HRE-rich shells covering the majority of the areal fraction close to the magnet surfaces, as observed by Kim et al. [23]. Therefore, it is reasonable to assume that both mechanisms are contributing to the formation of the final core-shell microstructure at the GBDP temperatures, which are higher than the eutectic temperature for the Nd-Fe-B system. As a result, the coercivity of a GBDP magnet can be strongly influenced by the dominant formation mechanism, which controls the resulting core-shell microstructure.

Systematic studies that would unequivocally determine the dominant core-shell formation mechanism and its implication for the final bulk magnetic properties are lacking. This is partly

influenced by the fact that the majority of the analytical work reported in the literature has been relying solely on advanced compositional and structural characterizations, where the resulting magnetic properties were deduced rather than directly assessed. This is a serious challenge for the required technology breakthrough in PM production that targets higher coercivities and maximum energy products in Nd-Fe-B.

To provide directions for the fabrication of GBDP magnets with minimum amounts of HRE, which can contribute to the outstanding increase of coercivity, but not at the expense of a lower remanent magnetization, we have used advanced correlative analytical electron microscopy (AEM) and atom-probe techniques to combine the structural and compositional information with spatially resolved magnetic imaging to quantitatively assess the nano-scale magnetic structure around the grain and core-shell boundaries in a Tb-treated, GBDP, Nd-Fe-B sintered magnet. To achieve this goal, in correlation with AEM, off-axis electron holography and Lorentz microscopy in magnetic-field-free conditions were conducted to observe the magnetic structures in the Tb-treated, GBDP, Nd-Fe-B magnet [26, 27], particularly near the core-shell interface and close to the shell-GB region. The complete, spatially resolved, correlative structure-chemistry-magnetism property analysis of the PMs provides enough data to propose a dominant core-shell formation mechanism and the resulting optimum core-shell structure. This gives clear directions for future fabrication techniques that can lead to a new, greatly improved, generation of permanent magnets.

## 1. Experimental

Two differently processed magnets, both purchased from Shinetsu Chemical Co., were used in this study. The magnets were rectangular in shape with dimensions of $17 \times 17 \times 2$ mm. The first sample was a commercial, as-sintered, Nd-Fe-B magnet, free of Tb. The second sample was a commercial, as-sintered, Nd-Fe-B magnet doped with Tb using the GBDP. This latter

sample will be denoted as *GBDP Nd-Fe-B*. It was produced (at Shinetsu) by applying a slurry of $Tb_4O_7$ particles to the surface of as-sintered Nd-Fe-B magnets, which were subsequently heated at 850 °C for 10 h, followed by a post annealing at 500 °C for 1 h in vacuum. To clearly differentiate the influence of the Tb and that of the additional heat treatment on the resulting magnetic properties, the as-sintered Nd-Fe-B magnet (hereafter denoted as *non-GBDP Nd-Fe-B*) was subjected to the same heating regime (in our laboratory) as the *GBDP Nd-Fe-B* magnet, i.e., heated at 850 °C for 10 h, followed by a post annealing at 500 °C for 1 h in a vacuum atmosphere.

Fig. 1 shows the schematics of the specimen-preparation procedure for the *non-GBDP Nd-Fe-B* and *GBDP Nd-Fe-B* magnets. Both magnets were initially cut into 16 equal pieces of 4 × 4 × 2 mm. The central piece, extracted from both magnets, was subsequently cut into 5 additional slices of 4 × 4 × 0.3 mm, perpendicular to the magnet surface, the direction of the Tb diffusion and the easy axis of magnetization. For the microstructure analysis, the 1st and 3rd slices of the *GBDP Nd-Fe-B* magnets were used for the further extraction of specimens from selected regions of interest (marked as ROIs). Note that the 1st slice is characterised by its $Tb_4O_7$ surface deposition, while the 3rd slice represents the central region of the magnet. TEM lamellae were extracted from four different ROIs, ROI 1–3 and ROI 4 from the 1st and 3rd slices, respectively. ROI 1 represents the surface region where detailed scanning electron microscopy combined with energy-dispersive x-ray spectroscopy (SEM-EDXS) and transmission electron microscopy combined with electron-energy-loss spectroscopy (TEM-EELS) analyses of the magnet surface were performed. For a detailed TEM-EELS analysis of the core-shell boundaries and the surrounding microstructure close to the surface, ROI 2 was selected at a depth of ~5 µm into the magnet from the surface. ROI 3 was at a depth of ~100 µm into the magnet. A needle-shaped specimen for the 3D atom probe (3DAP) was extracted for a detailed compositional characterization, while the TEM lamella was used for the analysis of the spatially

resolved magnetic properties by applying Lorentz microscopy and EH focused on the core-shell matrix-grain regions. The detailed TEM-EELS analysis of the grain-boundary composition and the EH was performed on ROI 4, which came from a depth of approximately 1000 μm into the magnet.

The demagnetization curves of the bulk magnets and the corresponding individual slices were measured using a Lakeshore vibrating-sample magnetometer (VSM). Since the intrinsic coercivity values of the *GBDP Nd-Fe-B* samples at room temperature exceed the maximum demagnetization field of 1200 kA/m that can be supplied by the VSM, the magnetic measurements were performed at 70 °C, allowing a complete demagnetization of the analysed samples, and the coercivity values were extracted for that temperature.

The bulk chemical compositions of the 1st and 3rd slices from the *GBDP Nd-Fe-B* magnet were determined by applying inductively coupled plasma optical emission spectroscopy (ICP-OES) (Varian, Model 715-ES). The relative experimental uncertainty for the ICP-OES conditions was around 5 %.

The microstructures and chemical compositions of the *GBDP Nd-Fe-B* magnet samples were analysed using a high-resolution, field-emission-gun SEM (FEG-SEM) JEOL JSM-7600F equipped with an Oxford Instruments INCA Energy350/Wave500 system for EDXS. TEM lamellae and needle-shaped specimens for the 3DAP analyses were fabricated in a dual-beam FIB-SEM (Thermo Fisher, Helios Nanolab 400) using a $Ga^+$ focused-ion-beam (FIB) milling procedure, with the ion energies set between 5 to 30 keV, combined with a conventional lift-out method using an OmniProbe™ tip. The ion-beam-induced artefacts were reduced by applying low-energy (<1 keV) Ar-ion-beam milling using a Fischione Nanomill system [28].

For the detailed structural and compositional investigations, a field-emission (scanning) TEM/STEM (JEM-2010F) operated at 200 keV (Cs = 0.48 mm) equipped with bright-field (BF) and high-angle annular dark-field (HAADF) detectors, EDXS (LINK ISIS EDS 300) and

an EELS (Gatan PEELS 766) system was applied. The probe size in the STEM was 1.5 nm. The probe convergence and collection semi-angle were set to 20 mrad. The compositional, structural and spatially resolved magnetic properties of the specimens from ROI 3–4 were studied using a spherical-aberration-corrected scanning-transmission electron microscope (ThermoFisher Titan 80-200) operated at 200 kV and equipped with an in-column energy-dispersive X-ray spectrometer and an electron-energy-loss spectrometer (Gatan Enfinium). The EDXS spectra images were collected and processed using Bruker Esprit software. The probe size in the STEM was around 0.1 nm. The probe convergence and collection semi-angle were 25 and 33 mrad, respectively.

To achieve a reliable quantitative analysis for the elements under investigation, a customized analytical procedure for the EELS analysis was developed. To enhance the signal-to-noise ratio of the intrinsically weak edges, such as Tb-$M_{4,5}$, the channel-to-channel noise fluctuation was reduced by applying principle component analysis (PCA) [20, 29]. Since the theoretically calculated partial cross-section values for the given ionization edges can result in an approximately 20% relative uncertainty, we improved the accuracy by choosing $Nd_2Fe_{14}B$ and $Tb_2Fe_{14}B$ reference materials to extract the experimental cross-section ratios for the $\sigma_{Nd}/\sigma_{Fe}$ and $\sigma_{Tb}/\sigma_{Fe}$, respectively. The corresponding EELS spectra for the $Nd_2Fe_{14}B$ and $Tb_2Fe_{14}B$ are presented in Supplementary Fig. 1. The average $\sigma_{Nd}/\sigma_{Fe}$ and $\sigma_{Tb}/\sigma_{Fe}$ values acquired from more than a dozen spectra for the JEM2010F's experimental conditions were 0.44 and 0.97, respectively. The resulting relative uncertainty in the experimental cross-section ratios was 2–3 %. The same experimental cross-section ratios were used for quantitative analyses of the EELS spectra acquired from the ThermoFisher Titan 80-200. The estimated relative uncertainty, taking into account the slightly different probe collection and convergence semi-angles, was around 1 %, which is significantly lower in comparison with the given confidence limits for the experimental cross-section ratios. It turned out, experimentally, that the largest

source of uncertainty was the plural scattering effect, which correlates with the thickness variations between the analysed samples.

The magnetic microstructures of the TEM specimens were studied in magnetic-field-free conditions (Lorentz mode) using a spherical-aberration-corrected TEM (ThermoFisher Titan 60-300) operated at 300 kV. Fresnel defocused images and off-axis electron holograms were recorded with direct electron-counting detectors (Gatan K2 IS) [30]. The electron holograms were acquired using a single-electron biprism inserted into one of the conjugated image planes of the microscope. The images were processed using custom-made software based on Semper [31]. The 3DAP was performed on a needle-shaped specimen in laser-evaporation mode using the 3D atom probe LEAP 4000x HR system from CAMECA. The estimated relative error for the measured elements was below 10%.

## 2. Results

The measured coercivity of the *GBDP Nd-Fe-B* magnet before cutting was 1048 kA/m (at 70 °C), a value which is ∼40 % higher than for the *non-GBDP Nd-Fe-B* magnet. In contrast, the overall remanent magnetization of the *GBDP Nd-Fe-B* magnet was only 1 % lower than the *non-GBDP magnet* (at 70 °C), which had a value of $M_r=1.35T$.

Fig. 2 (a) shows the differences in the coercivity between the individual slices, with relatively constant coercivity values of 738±4.6 kA/m (for all the measured slices) and greatly varying U-shaped values ranging from 983 (3rd slice) to 1100 kA/m (1st and 5th slice) for the *non-GBDP Nd-Fe-B* and *GBDP Nd-Fe-B* magnets, respectively. The highest coercivity values are associated with the surface slice (1st and 5th slice), which are approximately 40 % higher than the values measured for the *non-GBDP Nd-Fe-B* magnet. The coercivity values measured for the inner slice gradually decrease as we move away from the magnet's surface, reaching the lowest value in the central slice (3rd slice). A different trend is observed for the remanent

magnetization with respect to the *non-GBDP Nd-Fe-B* and *GBDP Nd-Fe-B* magnets, see Fig. 2 (b). While the remanent-magnetization values measured for individual slices for the *non GBDP Nd-Fe-B* magnet were practically the same, i.e., 1.35±0.5 T, the values for the *GBDP Nd-Fe-B* magnet fit a reversed A-shape curve of the remanent magnetization vs. slice number varying from 1.31 T to 1.35 T, characteristic for the $1^{st}$ and $5^{th}$ slices, respectively. The lowest remanent magnetization values are associated with the surface slice, with values increasing towards the centre of the magnet. Interestingly, the remanent magnetization value for the central, i.e., $3^{rd}$, slice is identical to the *non-GBDP Nd-Fe-B magnet,* although the associated increase in coercivity is still 30% higher than that of the *non-GBDP Nd-Fe-B* magnet.

The overall compositions of the $1^{st}$ and $3^{rd}$ slices of the *GBDP Nd-Fe-B* magnet were determined by ICP-OES analysis. The amount of Fe is very similar in both slices, 84±4 at.% and 83±4 at.%, respectively. In the $1^{st}$ slice the concentration of Nd is $14.2 \pm 0.7$ at.% and that of Tb is $0.88 \pm 0.04$ at.%. The characteristic Nd concentration for the $3^{rd}$ slice is 14.9±0.8 at.% and Tb $0.14 \pm 0.01$ at.%. According to this, the Tb concentration in the $3^{rd}$ slice amounts to around 15% of the Tb present in the $1^{st}$ slice.

Fig. 3 (a) shows a back-scattered electron (BSE) SEM image in cross-section view of the surface area of a *GBDP Nd-Fe-B* magnet acquired from ROI 1. The left-hand image is the top magnet surface in a cross-section view, where the $Tb_4O_7$ particles were deposited. The diffusion direction of the Tb from the surface into the interior of the magnet is indicated by an arrow. The overall microstructure of the $1^{st}$ slice, if compared to the conventional as-sintered and non-GBDP Nd-Fe-B magnet, is characterized by the so-called core-shell structure superimposed on the $Nd_2Fe_{14}B$ matrix grains. The contrast variations of the BSE-SEM images suggest that the shell is richer in Tb compared to the core regions of the parent crystal grains. The representative corresponding EDXS analyses that were performed on the shell and core regions from several grains confirm the composition of $(Nd_{0.54},Tb_{0.46})_2Fe_{14}B$ and $Nd_2Fe_{14}B$, respectively. A further

analysis of the core-shell-dominated microstructure shows that the shell thickness gradually decreases from the surface into the magnet interior. Namely, the specimen's surface region is characterised by a shell thickness of up to 2 μm, reaching values of about 100 nm at a depth of approximately 100 μm from the surface of the magnet. At greater depths in the 1st slice the core-shell structure is no longer visible when using BSE-SEM imaging. No significant differences in the overall microstructure between the *non-GBDP Nd-Fe-B* magnet and the 3rd slice of the *GBDP Nd-Fe-B* magnet could be observed using the SEM.

In contrast to the *non GBDP Nd-Fe-B*, the *GBDP Nd-Fe-B* magnet's surface is characterized by a non-uniform layer composed of brighter grains when observed in cross-section using BSE-SEM imaging. Although it would be reasonable to assume that these layers are mainly the remnants of $Tb_4O_7$ particles, the corresponding EDXS analyses indicate predominately a Nd-rich oxide phase with the partial substitution of Nd with Tb and Fe.

A more detailed analysis was performed with analytical transmission electron microscopy, combining a conventional TEM and HAADF-STEM imaging with quantitative EELS spectroscopy. Fig. 3 (b) shows the BF-TEM image of a representative Nd(Tb,Fe)-rich grain from the described oxide surface layer. The observed grain is crystalline, based on electron diffraction experiments, and it contains a high density of dislocations and inclusions with a nodular morphology. Fig. 3 (c) shows a HAADF-STEM image of these inclusions, indicating that they are different in terms of composition when compared to the parent oxide phase. Some inclusions are represented by an onion-like structure. To assess the compositional variations from such inclusions, EELS elemental concentration line scans were performed. A representative line scan indicated by the line in Fig. 3 (c) is shown in Fig. 3 (d). The line scan was acquired from the central part of the onion-like nodular inclusion into the parent oxide phase. Three compositionally distinct regions were subtracted from this measurement. The average composition of the parent oxide phase contains approximately 10±0.5 at.% of Fe,

35±0.9 at.% of Nd, 5±0.3 at.% of Tb, and 42±1.5 at.% of O. The outer skirt of the inclusion shows a reversed composition of rare earths when compared to the composition of the parent oxide, i.e., 35±0.8 at.% of Tb and 5±0.2 at.% of Nd. In the central part of the inclusion the composition of rare earth (Nd, Tb) is equilibrated to 20±0.6 at.%. The concentration of Fe is not significantly changed across the inclusion, while the amount of O is slightly higher when compared to the adjacent matrix.

A detailed compositional and nano-structural analysis of the core-shell grain from the ROI 2 is presented in Fig. 4 (a). The larger section of the presented high-resolution TEM (HRTEM) image is occupied by a $Nd_2Fe_{14}B$ matrix grain viewed along the <001> zone axis, as confirmed by the corresponding SAED pattern analysis (shown in the rectangular insets). The round-shaped phase (oxide phase), from which one part is shown in the right-hand section of the image, is approximately 1.5 μm in size. The EELS spectra from three different image regions marked by roman numerals (I, II, III) are shown in Fig. 4 (b). The round-shaped phase (Sp-I) is an oxide, characterized by Nd (50±1 at.%), Tb (8±0.4 at.%), Fe (16±1 at.%) and O (26±1 at.%). Spectra Sp-II and Sp-III were 200 nm apart in the $Nd_2Fe_{14}B$ matrix grain. Although the spectrum features are very similar, Sp-III has an additional spectrum feature at 1241 eV, which is significant for the $Tb-M_{4,5}$ ionization edge.

More detailed compositional variations in the Nd-Fe-B grain were investigated by a series of EELS elemental maps and line scans. A representative EELS elemental map was acquired from the region partly occupying the $Nd_2Fe_{14}B$ matrix grain and the oxide phase, as marked by the $250 \times 250$ nm$^2$ rectangle (R1) in Fig. 4 (a). The analytical pixel size was 25 nm. The superimposed $Fe-L_{2,3}$, $Nd-M_{4,5}$ and $Tb-M_{4,5}$ signals are in red, green and blue, respectively. The superimposed elemental map clearly shows the different compositions of the oxide phase (in blue) and the adjacent $Nd_2Fe_{14}B$ matrix grain. The different concentrations of Tb in this grain are shown by two colours. The red represents the pure $Nd_2Fe_{14}B$, while the orange indicates the

presence of some Tb, which is consistent with the core-shell structure of the matrix $Nd_2Fe_{14}B$ grains. In addition, the core-shell boundary is nearly perpendicular to the phase boundary between the Nd(Tb,Fe)-rich oxide (blue) and $(Nd,Tb)_2Fe_{14}B$ matrix phase (orange/red). As the Tb-free core region of the matrix grain neighbours the Tb-containing oxide phase, it is possible that in this particular case the source of Tb for the shell formation in the matrix grain did not originate from the adjacent Tb-containing oxide phase.

The crystallographic orientation of the core-shell boundary in relation to the underlying crystal structure of the Nd-Fe-B matrix grain was deduced from a fast Fourier transform (FFT) acquired from the shell and the core region. The FFT caries information about the spatial frequencies from the analysed image region and can be (to a first approximation) correlated with the information obtained from the corresponding SAED pattern. No significant difference can be observed for these two FFTs, which indicates that the core and the shell are crystallographically identical. Moreover, the corresponding HRTEM image from the core-shell boundary region did not reveal any structural peculiarities, such as dislocations or other types of planar faults. The normal of the core-shell boundary, i.e., the growing direction of the shell, is close to the (100) crystallographic direction, relative to the underlying $Nd_2Fe_{14}B$ matrix crystal.

Fig. 5 shows a detailed compositional profile of the core-shell boundary performed by an EELS line-scan with a point-by-point resolution of 1.8 nm. The line scan shows the nearly constant concentration of Nd (6±0.7 at.%) and Tb (2±0.4 at.%) in the shell, while the transition region from the shell to the core is indicated by a rapid decrease of the Tb concentration to zero, i.e., below the detection limit for this EELS analysis (0.4 at.%). The width of the rapidly decreasing Tb concentration profile was about 20 nm.

The 3D distribution of the individual elements around the characteristic core-shell region from ROI 3 was reconstructed using a 3D atom-probe (3DAP) tomography experiment, as

shown in Fig. 6. The elemental maps in Fig. 6 (a) show the distributions of Fe, Nd and Tb in the analysed needle-shaped specimen. The concentration of Fe is constant over the whole map, while the Nd and Tb are exchanging across the core-shell region. More specifically, the top part of the needle-shaped elemental map shows the presence of Tb, indicating the shell region of the matrix grain. The lower part of the needle is characteristic of the $Nd_2Fe_{14}B$ core. The elemental line scan was extracted from the obtained tomograms, perpendicular to the core-shell boundary, as indicated in Fig. 6 (b). The corresponding calculated concentration profiles for Nd and Tb are shown in Fig. 6 (c). The concentrations of Nd and Tb are comparable to the concentrations obtained using the EELS analysis in Fig. 5. The line profile shows a nearly constant concentration of Nd (9.3±0.3 at.%) and Tb (3.3±0.2 at.%) in the shell, while the transition region from the shell to the core is characterised by a rapid decrease in the Tb concentration to zero, i.e., below the detectability limits of the 3DAP analysis (0.2 at.%). The width of the rapidly decreasing Tb concentration profile was 10 nm.

Fig. 7 (a) shows a HAADF-STEM image of the GB region acquired from ROI 4, which is approximately 1000 μm from the magnet's surface in its central part. EDXS analyses (Supplementary Fig. 2) showed that Tb is mainly concentrated at the Nd-rich triple points (TPs). EELS line-scan analyses of the GBs and the adjacent $Nd_2Fe_{14}B$ matrix grains were made to determine the concentration distribution of the Tb, specifically in the GB regions. Only the GBs parallel to the electron beam (*edge on*) were selected for a detailed analysis. The correct orientation of a particular GB was identified by assessing the intensity distribution related to the Fresnel diffraction at the boundary. Accordingly, the GBs where the Fresnel contrast was symmetrical along the boundaries, indicating the *edge-on* condition, were selected for further analyses. A typical *edge-on* GB region, where the EELS line-scan analysis was performed, is shown in the inset of Fig. 7 (a). The line-scan width was set to 30 nm, with a pixel resolution of 0.3 nm. The resulting concentration profiles are presented in Fig. 7 (b). The concentration

distributions of Fe and Nd are complementary. They are relatively constant in both matrix-grain regions. At the GB a significant drop in the amount of Fe is correlated with an increase in the concentration of Nd. The composition of the GB in its central region corresponds to Fe (80.5±1.1 at.%), Nd (18±1.1 at.%) and Tb (1.6±0.3 at.%). The chemical width of the GB, deduced from the concentration profile of Fe and Nd, is 7 nm. In contrast, the Tb concentration profile shows a different distribution, not bound to the GB region, but extending approximately 10 nm into the interior of the adjacent matrix grains. In contrast to the concentration profiles measured in the core-shell matrix-grain regions (ROI 2), where the Tb concentration was nearly constant over the whole shell, here the Tb concentration starts to decrease from the GB region into the adjacent matrix grains.

Fig. 8 shows the magnetic imaging studies of the *GBDP Nd-Fe-B* magnet prepared from ROI 3. The BF-STEM image in Fig. 8 (a) shows the grain structure within the specimens. The core-shell structure in the specimen is confirmed by the contrast variation due to the concentration changes in Nd and Tb (Supplementary Fig. 3). The Fresnel defocused image reveals a complex network of magnetic domain walls (DWs), as shown in Fig. 8 (b). It is striking that the shell regions are characterised by a low density of DWs, or no DWs, while the DW density is high within the core. Fig. 8 (c) shows the total electron optical phase shift $\phi$ map, extracted from the off-axis electron-holography experiment carried out in remanence mode, which contains the contributions of the magnetic phase shift $\phi_m$ and the mean inner potential (MIP). The magnetic DWs appear as black and white contrast maxima and minima in the phase-shift image. The edge region of the specimen, which is marked with a dashed white line, was damaged by the ion sputtering during the FIB specimen preparation procedure and was not included in the analysis. The magnetic phase shift $\phi_m$ was separated from the MIP by turning the specimen over, recording a second set of electron holograms and taking half the difference of the two total phase images. The magnetic phase image is directly proportional to

the in-plane component of the magnetic induction within and around the specimen integrated into the electron beam direction [32]. Fig. 8 (d) shows the magnetic phase slope, characterized by the three walls, perpendicular to the core-shell boundary, as marked by an arrow in Fig. 8 (c). The phase slope that corresponds to the in-plane magnetic induction in the sample was calculated for the core and shell regions as 0.06±0.005 and 0.047±0.005 rad/nm, respectively. The difference in the slopes indicates that the magnetic induction in the core is approximately 26 % higher than that of the shell. Fig. 8 (e) shows a visual representation of the projected in-plane magnetic field, which can be obtained by adding contours and colours, for example, by evaluating the cosine of a chosen multiple of the magnetic phase image and the derivatives. The core-shell boundary and the GB are indicated by the red and green dashed lines, respectively. The colours and field-lines arrangements at the DW locations indicate close-to-180º DWs at the boundary of the shell and inside the core region. The field lines form flux closures at the top of the magnetic induction map close to the edge of the TEM specimen.

By analysing the differential of the magnetic phase $\phi_m$(x), the width of the domain walls in the core and across the core-shell boundary is determined, as shown in Fig. 9. The step function across the DW is defined by the expression $y=y_0\pm atanh((x-x_0)/w)$, where $y_0$, $a$ and $w$ are constants obtained from the fit. Then the DW width $\delta_w$ is determined as $\delta_w=\pi w$. The $\delta_w$ measured for the DWs located at the core-grain region and the core-shell boundary are 4.5±1.6 nm and 4.0 nm ±1.6 nm, respectively.

Fig. 10 shows magnetic imaging studies of the central region of the *GBDP Nd-Fe-B* magnet (ROI 4), which is exactly the same specimen region as shown in Fig. 7. The Fresnel defocused image shown in Fig. 10 (a) reveals the presence of straight-line magnetic DWs. Interestingly, two of the grain boundaries overlap perfectly with the DWs, suggesting a strong pinning effect. The magnetic induction map in Fig. 10 (b) shows the directional change of the magnetic field at the DWs and GBs. Many of the DWs have a perfect 180º magnetic field rotation between the

domains. The magnetic state around the grain boundary on the right-hand side is rather complex, showing flux reversal on both sides of the boundary. Note that the exact magnetic state cannot be fully recovered as the off-axis electron-holography experiment provides information on the in-plane field components, while the out-of-plane component remains undetected. The $\delta_w$ measured for the DWs located at the core-grain region was 5.4±1.1 nm, as shown in Fig. 10 (c).

### 3. Discussion

The highest coercivity of the studied *GBDP Nd-Fe-B* magnet is associated with the 1st slice, which was initially in contact with $Tb_4O_7$ particle slurry. This slice is characterised by the highest density of core-shell-structured matrix grains close to the surface. The average thickness of the Tb-rich shells within these matrix grains decreases rapidly towards the specimen's interior and cannot be traced across the whole of the 1st slice. This is even more evident in the central, i.e., 3rd, slice, where the differences in the microstructure between the *non-GBDP* and *GBDP Nd-Fe-B* magnets cannot be revealed by means of SEM.

The ICP-OES analysis indicates that the overall concentration of Tb in the central slice is only 15 % of the value measured in the surface slices. This sharp drop in the Tb concentration is even more pronounced if we consider that only the Tb present in the Nd-Fe-B matrix grains contributes to the increase in the coercivity for the analysed slices. To determine the total amount of Tb that is present in the Nd-Fe-B matrix grains within the central slice (the 3rd slice) we assumed the uniform concentration profile shown in Fig. 7 (b) and an average matrix-grain size of 5 μm, which was deduced from the corresponding SEM images and was approximated to a perfect cube. The total amount of Tb in the Nd-Fe-B matrix grains was calculated to be 0.005 at.%. The implication is that in the ideal case only 50 ppm of Tb doped in the Nd-Fe-B magnet is sufficient for a drastic 30 % increase in the coercivity, when compared to the *non-*

*GBDP Nd-Fe-B* magnet. Moreover, a much greater concentration of Tb in the surface slices contributes only an additional 25 % improvement in the coercivity, i.e., from 30 % to 40 %, which implies that the majority of the Tb in the surface slices is not contributing to the coercivity improvement.

Another important, and so-far overlooked, phenomenon that dictates the overall core-shell evolution of the GBDP magnets is related to the different starting precursors for the HREs, i.e., metal, hydride, fluoride or oxide. For the Tb case, the exact melting point for $Tb_4O_7$ has not unambiguously determined, as the Tb-O phase diagram has only been partially investigated. Nevertheless, the Tb-O phase diagram between 60.0 and 67.0 at.% oxygen shows the presence of $Tb_2O_3$, $TbO_2$ and $Tb_7O_{12}$, all in the solid state and with no liquid forming below 1200 °C, which is much higher than the processing temperatures in this study [33]. Our results, as in Figs. 3 and 4, clearly show that the GBDP provokes the formation of a Nd-rich-oxides layer with minor amounts of Tb and Fe in the very surface regions of the magnet. In a very simplified picture, this can be explained by the electro-reduction potential of the lanthanides, as follows: Nd: $Nd^{3+} + 3$ e− $\rightleftharpoons$ Nd ($E_0$=−2.323 V), Dy: $Dy^{3+} + 3$ e− $\rightleftharpoons$ Dy ($E_0$=−2.295 V), Tb: $Tb^{3+} + 3$ e− $\rightleftharpoons$ Tb ($E_0$=−2.28 V), which implies that the Nd in a zero-oxidation state is a strong-enough reducing agent at elevated temperatures to reduce other lanthanides (Ln) to Ln (0) by self-oxidation, possibly via $Tb_4O_7 + 5Nd \rightarrow 2Nd_2O_3 + 4Tb + NdO_{1-x}$. So, most probably in a close contact between $Tb_4O_7$ and metallic Nd, originating from either the Nd-rich GB phases or the Nd-Fe-B matrix, the equilibrated system will favour the oxidation of Nd combined with the consequent reduction of Tb from the corresponding oxide. This exchange mechanism is clearly observed in Fig. 3 (d), where only the Nd atoms are completely exchanged with the Tb, whereas the Fe and O remain almost constant. In reality, the system is probably more complex, as it contains matrix $Nd_2Fe_{14}B$ grains, trapped oxygen at the specimen's surface, and various GB and TP phases. We can thus anticipate a cascade of chemical reactions between the Tb oxide

and Nd and/or $Nd_2Fe_{14}B$ to various multicomponent oxides, which gradually decrease the oxidation state of the Tb. As seen in Figs. 3 (c) and (d), the crystal matrix surrounding the onion-like inclusions is rich in O and Nd and lean in terms of Fe and Tb, with the B not being accounted for. That would change the composition of both the inclusions as well as the adjacent matrix to some extent. According to the most plausible phase equilibria [34], the matrix grains lying just below the Tb-rich coating are made of complex multicomponent oxides based on $Nd_4B_2O_9$. The inclusions, on the other hand, are actually the remnants of the formation of the complex $Nd_4B_2O_9$-type oxide, which was initially formed step-wise from simpler stable oxides like $NdB_3O_6$ and $FeB_4O_7$. Namely, these two types of oxides are more stable than $Tb_2O_3$ (-4,007 eV/unit-cell formation energy required) and $Nd_2O_3$ (-3,765 eV/unit-cell formation energy required) for instance with formation energies of -6,059 eV/unit cell for $NdB_3O_6$ and -5,912 eV/unit cell for $FeB_4O_7$, where the $Nd_4B_2O_9$ is the most stable with -10,395 eV/unit cell [34]. In summary, the oxygen-rich phase-equilibrium system when combined with Nd, Fe and B predicts certain end-member equilibrium phases, which suggests that the proposed exchange mechanism favours the formation of a cascade of oxides. Once the Tb is released by the above-described mechanisms from the precursor compounds, it can diffuse along the GBs, thus forming the initial reservoir for the later formation of Tb-rich shells within the matrix Nd-Fe-B grains. It is likely that different HRE precursors will experience different cascades of chemical reactions, where the overall reaction kinetics will dictate the amount of free HRE for the final core-shell formation during the GBDP. The intermediate state, where the Nd(Fe,Tb)-rich oxides and Nd-Fe-B core-shell-structured matrix grain coexist in close proximity, is presented in Fig. 4 (a). The related results on the spatially resolved chemistry obtained from that specimen area, which is only 5 µm below the magnet surface, are in accordance with the above-described gradual release mechanism for Tb, as it is evident that Tb is not directly diffusing into the Nd-Fe-B matrix grains from the adjacent Nd(Fe,Tb)-rich oxide.

The explanation of the dominant mechanism that controls the formation of the core-shell microstructure in the studied system relies on the two generally accepted core-shell formation models for the GBDP HRE-based sintered magnets. In the first one, the HRE is diffusing along the GBs as a part of the liquid GB phase above the ternary eutectic temperature (~685 °C) [22], which is accompanied by the partial melting of the $Nd_2Fe_{14}B$ matrix grains. Upon cooling below the solid/liquid phase line the $(HREE,Nd)_2Fe_{14}B$ shells will precipitate out of the liquid phase and condense on the surface of $Nd_2Fe_{14}B$ grains [16, 21-23, 35, 36]. The resulting composition of the shells should show the nearly constant concentration of the HREs, which is to some extent in accordance with our observations in Figs. 5 and 6 (c). The GBDP temperature in this study is above the reported ternary eutectic temperature. From that perspective it is reasonable to assume that the core-shell formation was following the first model.

However, a more detailed analysis of our results may not adhere entirely to this theory, as it was revealed that at 5 µm from the surface the core shell-boundary is structurally, perfectly coherent, and free of planar defects. This is not typical for a chemically induced, liquid-film migration mechanism [23]. Moreover, a detailed analysis of the core-shell boundary reveals that the drop in the Tb concentration is not abrupt, as it is always associated with a diffusion profile with a thickness of between 10 and 20 nm. These observations are more easily explained by the second model, which is based on the solid-state diffusion of the HRE along the GB, driven below the ternary eutectic temperature, as reported by Loewe et al. [18] and Kim et al. [24] To be exact, as we move further away from the surface of the magnet, the Tb reservoir, i.e., the GB phases, are increasingly depleted of Tb. Moreover, the GBDP for Tb becomes even more difficult once the $(Nd,Tb)_2Fe_{14}B$ shells are formed, as they are less susceptible to the substitutional diffusion of Tb. As a consequence, both the Tb concentration at the GBs and the thickness of the shells are rapidly decreasing as we move towards the interior of the GBDP magnet. As an extreme case, in the central region of the magnet (the 3rd slice), the amount of

Tb available to form a shell of constant concentration is much too small, and thus it remains bound to a thin diffusion region (10 nm) along the GBs. Another argument that supports the idea that diffusion is dominating over the chemically induced liquid-film migration for the incorporation of Tb into the Nd-Fe-B matrix grain, also in accordance with the Kim et al. [23], is related to the fact that the liquid/solid phase equilibrium does not accommodate the observed amounts of Tb-rich areas near the magnet surface, covering more than 50 % of the areal fraction. This could imply that the generally accepted eutectic temperature determined in the pseudo-binary Nd-Fe-B phase diagram [22] is underestimated for the studied system and that the experimental temperature of 850 °C might be just below the eutectic point, which would preserve the GBs in their solid state.

Magnetic imaging studies were performed in parallel with the surface-chemistry studies of the Nd-Fe-B grains. The off-axis electron-holography measurements indicated a 26 % higher magnetic induction in the core than that of the shell for ROI 3 of the *GBDP Nd-Fe-B* magnet (Fig. 8). The different values are explained by the fact that the magnetic saturation of $Nd_2Fe_{14}B$ is 1.6 T, while pure $Tb_2Fe_{14}B$ reaches only 0.7 T. It is plausible, therefore, to assume that a partial substitution of Nd by Tb in the shell will result in a reduced magnetic induction in the Tb-rich shell region. Such a direct comparison was possible to make when using a specimen that is characterised by having the same thickness in the core and shell regions. Another interesting observation is that the shell is magnetized in a single direction, so it does not exhibit either a magnetic-domain pattern or any DWs.

In a nucleation-controlled coercivity, as proposed by Givord et al. [37], the nucleation of a reverse domain starts at defects on the surface of the matrix grains, and as calculated by Bance et al. [38], a 3-nm-thick region around the individual $Nd_2Fe_{14}B$ grains of reduced magnetocrystalline anisotropy is enough to play a significant role in the overall coercivity of the bulk magnet. Spatially resolved variations of the magnetocrystalline anisotropy within the

core-shell structure, which can be related to the coercivity of the analysed slice, can be deduced from measurements of the magnetic DW width ($\delta_w$) by means of electron-holography measurements. Two adjoining magnetic domains with magnetisation forming an ideal 180° are separated by a DW that has a lateral dimension or width $\delta_w$ that is proportional to the square root of the exchange stiffness $A$ and inversely proportional to the effective anisotropy K: $\delta_w = \pi\sqrt{A/K}$. In other words, the competition between the exchange and anisotropy energies defines the wall configuration with the lowest energy. In $Nd_2Fe_{14}B$, the $\delta_w$ is 3.82 nm due to the high uniaxial anisotropy of the magnet. In an approximately 100-nm-thick TEM lamellae of $Nd_2Fe_{14}B$, the DW will have a Bloch configuration, i.e., the magnetic moments at the wall are aligned perpendicular to the moments in the domains. However, an accurate measurement of $\delta_w$ in permanent magnets is challenging due to the small dimensions. In this work we used magnetic phase maps to measure the $\delta_w$ in the *GBDP Nd-Fe-B* magnet where in ROI 3 the $\delta_w$ were 4.0 and 4.5 nm (Fig. 9) and in ROI 4 it was 5.4 nm (Fig. 10), which gives a good quantitative match with the values expected for $Nd_2Fe_{14}B$. Unfortunately, a better estimate of the DW width and, consequently, conclusions about the effect of Tb on the magnetic anisotropy from experimental measurements cannot be made without knowing the three-dimensional shape of the magnetic DW. The actual DW shape may have Néel components close to the surface where the long-range magnetostatic interactions try to force the magnetic moments to be inside the surface plane [39]. The different components would be superimposed in the projected Fresnel images and phase-shift maps, causing an overestimation of $\delta_w$. Presumably, this is the reason for measuring a $\delta_w$=5.4 nm in ROI 4 that was a thicker specimen (~100 nm) than that of ROI 3 (<70 nm). Interestingly, the shell region is characterised as a single magnetic domain, even across the grain boundaries, as shown in Fig. 8 (b). The lack of 180° DWs in the shell regions prevents an estimate of the magnetic anisotropy of the Tb-rich shell in the *GBDP Nd-Fe-B* magnet.

Taking this into account, we must not forget that the remanent magnetization in the $3^{rd}$ slice of the *GBDP Nd-Fe-B* magnet was not negatively affected by the presence of Tb. It can be assumed that the Tb distribution in the Nd-Fe-B grains is as characteristically presented in Fig. 7. Interestingly, this specimen region does not reveal a magnetic domain core-shell structure (Fig. 10 (c)). Therefore, a 30 % increase in the coercivity in that specimen slice cannot be satisfactorily explained by the presence of confined magnetic domains within the core and shell regions, which are characteristic of the $1^{st}$ slice (ROI 3 in Fig. 8). A nearly perfect match in the remanent magnetization of the *non-GBDP* magnet and the $3^{rd}$ slice of the *GBDP Nd-Fe-B* magnet possibly indicates the structural effect of Tb atoms on the coercivity, rather than a magnetic one, which is due to an enhanced spin-orbit coupling. In the case that a significant increase in the coercivity is dominated by the enhanced spin-orbit coupling, the remanent magnetization should also drop due to the associated anti-parallel coupling of the electronic spins between the transition metal and the HRE, as was measured in the $1^{st}$ slice (Fig. 2) and experimentally observed for the core-shell grains in ROI 3 (Fig. 8 (d)). Therefore, a substantial enhancement of the coercivity must originate from the absence of defects in the main Nd-Fe-B phase, which might be promoted by extremely small amounts of Tb atoms in the outmost surface layer of the Nd-Fe-B matrix grains.

## 4. Conclusion

Using correlative analytical electron microscopy with atom-probe techniques we combined structural and compositional information with spatially resolved magnetic imaging to study the nanoscale magnetic structure around the grain and the core-shell boundaries in a Tb-treated GBDP Nd-Fe-B sintered magnet. We observed that more than one mechanism is dictating the

growth of Tb-rich shells around the matrix Nd-Fe-B grains. On the surface where the Tb-oxide is deposited, GBDP causes the formation of Nd-rich oxide layers with a minor amount of Tb and Fe. With a cascade of chemical reactions between the Tb oxide and Nd and/or $Nd_2Fe_{14}B$ the $Nd_4B_2O_9$-type oxides are formed and the released Tb can diffuse along the GBs. We discussed two possible mechanisms, the chemically induced liquid-film migration mechanism and the solid-state mechanism. Taking into account the experimental results we observed that the core shell-boundary is structurally, perfectly coherent, free of planar defects and the drop of the Tb concentration on the core-shell boundary is not abrupt; it is also always associated with a diffusion profile. All these findings are in favour of the solid-state mechanism and it can be concluded that in the studied system the experimental temperature of 850 °C is below the eutectic point and the GBs are preserved in the solid state.

The concentration of Tb-rich shells in the *GBDP Nd-Fe-B* magnet decreases towards the central part of the magnet, but we still measured a 30 % increase of the coercivity compared to the *non-GBDP Nd-Fe-B* magnet. The calculations revealed that in an ideal case only 50 ppm of Tb doped in the Nd-Fe-B magnet is sufficient for this increase in coercivity.

Moreover, the off-axis electron-holography measurements showed a 26 % higher magnetic induction in the core compared to the shell, due to the lower magnetic saturation of $Tb_2Fe_{14}B$. Using magnetic phase maps, we experimentally measured the domain-wall width in the *GBDP Nd-Fe-B*, which gave a good quantitative match to the values expected for $Nd_2Fe_{14}B$. The lack of 180° domain walls (DWs) in the Tb-rich shell regions prevented us from measuring the DWs and estimating the magnetic anisotropy of the shells. Furthermore, the same value from the remanent magnetization of the *non-GBDP* magnet and the central part of the *GBDP Nd-Fe-B* magnet most probably shows the structural effect of the Tb atoms on the coercivity rather than a magnetic one, indicating that the increase in the coercivity must originate from the absence

of defects in the main Nd-Fe-B phase, which might be promoted by extremely small amounts of Tb atoms in the outmost surface layer of Nd-Fe-B matrix grains.

## References

[1] *https://ec.europa.eu/info/strategy/priorities-2019-2024/european-green-deal_en*.
[2] H. Nakamura, The current and future status of rare earth permanent magnets, Scripta Mater., 154 (2018) 273-276.
[3] *https://www.volkswagen-newsroom.com/en/press-releases/volkswagen-significantly-raises-electric-car-production-forecast-for-2025-5696*.
[4] D. Harimoto and Y. Matsuura, Development of high performance Nd–Fe–B sintered magnets, Hitachi Metals Technical Review, 23 (2007) 69-72.
[5] O. Gutfleisch, Controlling the properties of high energy density permanent magnetic materials by different processing routes, J. Phys. D: Appl. Phys., 33 (2000) R157.
[6] H. Sepehri-Amin, T. Ohkubo, T. Shima and K. Hono, Grain boundary and interface chemistry of an Nd–Fe–B-based sintered magnet, Acta Mater., 60 (2012) 819-830.
[7] A. Tiwari, *Magnetic nanostructured materials: from lab to fab*. 2018: Elsevier.
[8] K. Hono and H. Sepehri-Amin, Strategy for high-coercivity Nd–Fe–B magnets, Scripta Mater., 67 (2012) 530-535.
[9] M. Sagawa, S. Fujimura, H. Yamamoto, Y. Matsuura and K. Hiraga, Permanent magnet materials based on the rare earth-iron-boron tetragonal compounds, IEEE transactions on Magnetics, 20 (1984) 1584-1589.
[10] *https://www.arnoldmagnetics.com/wp-content/uploads/2017/10/Understanding-and-Using-Reversible-Temperature-Coefficients-Constantinides-Magnetics-2010-psn-hi-res.pdf*.
[11] J. Herbst, R 2 Fe 14 B materials: Intrinsic properties and technological aspects, Reviews of Modern Physics, 63 (1991) 819.

[12] H. Nakamura, K. Hirota, M. Shimao, T. Minowa and M. Honshima, Magnetic properties of extremely small Nd-Fe-B sintered magnets, IEEE transactions on magnetics, 41 (2005) 3844-3846.

[13] T. Komatsu, T. Sato, K.-i. Machida and H. Fukunaga. *IUMRS-ICA 2008 Symposium'AA. Rare-Earth Related Material Processing and Functions '*. in *IOP Conference Series: Materials Science and Engineering*. 2009. IOP Publishing, p. 011001.

[14] D. Li, S. Suzuki, T. Kawasaki and K.-i. Machida, Grain interface modification and magnetic properties of Nd–Fe–B sintered magnets, Japanese Journal of Applied Physics, 47 (2008) 7876.

[15] L. Zapf, K. Uestuener, R. Blank and M. Katter. *Proceedings of 20th international workshop on rare earth permanent magnet & their applications,* (2008) 83-86.

[16] M. Soderžnik, K.Ž. Rožman, S. Kobe and P. J. McGuiness, The grain-boundary diffusion process in Nd–Fe–B sintered magnets based on the electrophoretic deposition of DyF3, Intermetallics, 23 (2012) 158-162.

[17] K. Hirota, H. Nakamura, T. Minowa and M. Honshima, Coercivity enhancement by the grain boundary diffusion process to Nd–Fe–B sintered magnets, IEEE transactions on magnetics, 42 (2006) 2909-2911.

[18] K. Löewe, C. Brombacher, M. Katter and O. Gutfleisch, Temperature-dependent Dy diffusion processes in Nd–Fe–B permanent magnets, Acta Mater., 83 (2015) 248-255.

[19] M. Soderžnik, M. Korent, K.Ž. Soderžnik, M. Katter, K. Üstüner and S. Kobe, High-coercivity Nd-Fe-B magnets obtained with the electrophoretic deposition of submicron TbF3 followed by the grain-boundary diffusion process, Acta Mater., 115 (2016) 278-284.

[20] P. J. McGuiness, O. Akdogan, A. Asali, S. Bance, F. Bittner, J. Coey, N. Dempsey, J. Fidler, D. Givord and O. Gutfleisch, Replacement and Original Magnet Engineering Options (ROMEOs): A European seventh framework project to develop advanced permanent magnets without, or with reduced use of, critical raw materials, JOM, 67 (2015) 1306-1317.

[21] H. Sepehri-Amin, T. Ohkubo and K. Hono, The mechanism of coercivity enhancement by the grain boundary diffusion process of Nd–Fe–B sintered magnets, Acta Mater., 61 (2013) 1982-1990.

[22] U. Seelam, T. Ohkubo, T. Abe, S. Hirosawa and K. Hono, Faceted shell structure in grain boundary diffusion-processed sintered Nd–Fe–B magnets, J. Alloys Compd., 617 (2014) 884-892.

[23] T.-H. Kim, T. Sasaki, T. Koyama, Y. Fujikawa, M. Miwa, Y. Enokido, T. Ohkubo and K. Hono, Formation mechanism of Tb-rich shell in grain boundary diffusion processed Nd–Fe–B sintered magnets, Scripta Mater., 178 (2020) 433-437.

[24] T.-H. Kim, T. Sasaki, T. Ohkubo, Y. Takada, A. Kato, Y. Kaneko and K. Hono, Microstructure and coercivity of grain boundary diffusion processed Dy-free and Dy-containing NdFeB sintered magnets, Acta Mater., 172 (2019) 139-149.

[25] K. Loewe, D. Benke, C. Kübel, T. Lienig, K. Skokov and O. Gutfleisch, Grain boundary diffusion of different rare earth elements in Nd-Fe-B sintered magnets by experiment and FEM simulation, Acta Mater., 124 (2017) 421-429.

[26] Y. Zhu and M. McCartney, Magnetic-domain structure of Nd 2 Fe 14 B permanent magnets, J. Appl. Phys., 84 (1998) 3267-3272.

[27] Y. Murakami, T. Tanigaki, T. Sasaki, Y. Takeno, H. Park, T. Matsuda, T. Ohkubo, K. Hono and D. Shindo, Magnetism of ultrathin intergranular boundary regions in Nd–Fe–B permanent magnets, Acta Mater., 71 (2014) 370-379.

[28] P.E. Fischione, R.E. Williams, A. Genç, H.L. Fraser, R.E. Dunin-Borkowski, M. Luysberg, C.S. Bonifacio and A. Kovács, A small spot, inert gas, ion milling process as a complementary technique to focused ion beam specimen preparation, Microsc. Microanal., 23 (2017) 782-793.

[29] G. Lucas, P. Burdet, M. Cantoni and C. Hébert, Multivariate statistical analysis as a tool for the segmentation of 3D spectral data, Micron, 52 (2013) 49-56.

[30] S.L. Chang, C. Dwyer, C.B. Boothroyd and R.E. Dunin-Borkowski, Optimising electron holography in the presence of partial coherence and instrument instabilities, Ultramicroscopy, 151 (2015) 37-45.

[31] W. Saxton, T. Pitt and M. Horner, Digital image processing: the Semper system, Ultramicroscopy, 4 (1979) 343-353.

[32] A. Kovács and R.E. Dunin-Borkowski, *Magnetic Imaging of Nanostructures Using Off-Axis Electron Holography*, in *Handbook of Magnetic Materials*. 2018, Elsevier. p. 59-153.

[33] H. Okamoto and T. Massalski, Binary alloy phase diagrams, ASM International, Materials Park, OH, USA, (1990)

[34] L.K. Jakobsson, G. Tranell and I.-H. Jung, Experimental Investigation and Thermodynamic Modeling of the B2O3-FeO-Fe2O3-Nd2O3 System for Recycling of NdFeB Magnet Scrap, Metallurgical and Materials Transactions B, 48 (2017) 60-72.

[35] N. Oono, M. Sagawa, R. Kasada, H. Matsui and A. Kimura, Production of thick high-performance sintered neodymium magnets by grain boundary diffusion treatment with dysprosium–nickel–aluminum alloy, J. Magn. Magn. Mater., 323 (2011) 297-300.

[36] Z. Samardžija, P. J. McGuiness, M. Soderžnik, S. Kobe and M. Sagawa, Microstructural and compositional characterization of terbium-doped Nd–Fe–B sintered magnets, Mater. Charact., 67 (2012) 27-33.

[37] D. Givord, M. Rossignol and V.M. Barthem, The physics of coercivity, J. Magn. Magn. Mater., 258 (2003) 1-5.

[38] S. Bance, H. Oezelt, T. Schrefl, G. Ciuta, N.M. Dempsey, D. Givord, M. Winklhofer, G. Hrkac, G. Zimanyi and O. Gutfleisch, Influence of defect thickness on the angular dependence of coercivity in rare-earth permanent magnets, Appl. Phys. Lett., 104 (2014) 182408.

[39] E. Torok, A. Olson and H. Oredson, Transition between Bloch and Néel walls, J. Appl. Phys., 36 (1965) 1394-1399.

**Figures:**



Slice:
1 → ROI (1-3)
2
3 → ROI (4)
4
5

ROI 1: Surface (SEM/TEM/EELS)
ROI 2: 5 μm deep (TEM/EELS)
ROI 3: 100 μm deep (3DAP/EH)
ROI 4: 1000 μm deep (TEM/EELS/EH)
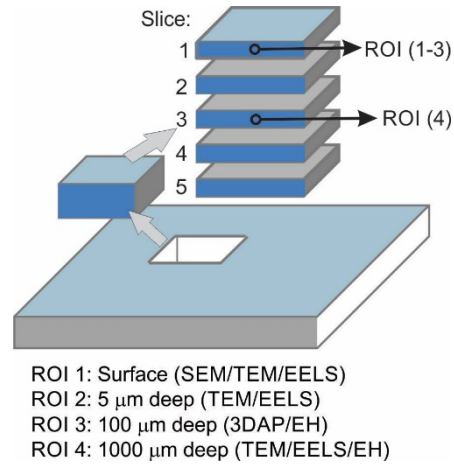
Figure 1. Scheme of cutting procedure for the investigated GBDP Nd-Fe-B magnet with indicated ROIs where the analysis was performed.
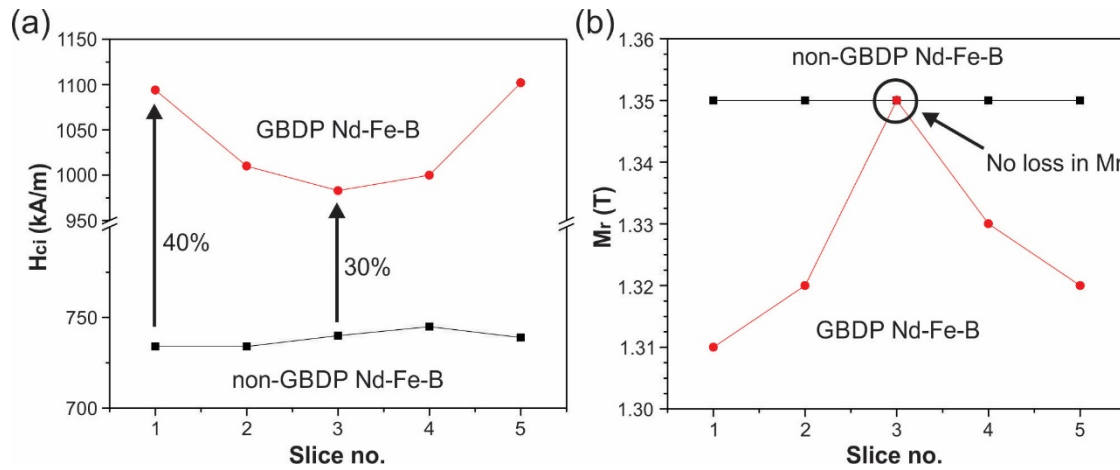


Figure 2. Lateral profiles of (a) coercivity ($H_{ci}$) and (b) remanent magnetization ($M_r$) at 70 °C. Black curve represents *non-GBDP Nd-Fe-B* magnet, red curve represents *GBDP Nd-Fe-B* magnet.
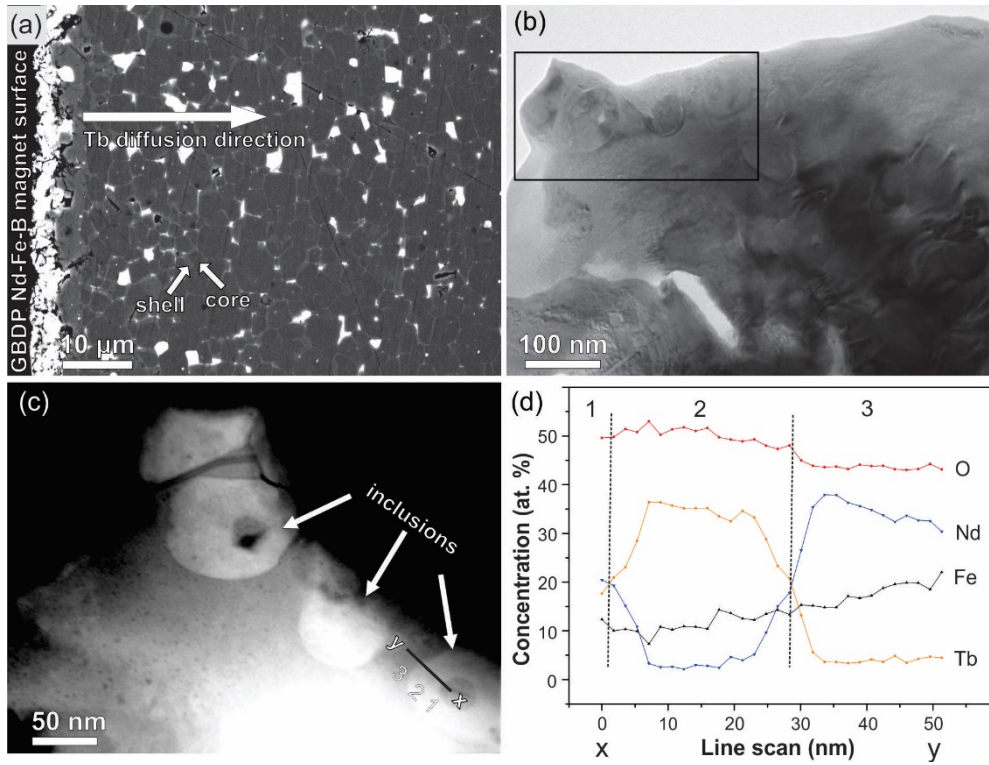
Figure 3. 1st slice of *GBDP Nd-Fe-B* magnet; (a) BEI-SEM image, (b) BF-TEM image of a representative oxide grain from ROI 1. (c) HAADF-STEM image of inclusions inside the Nd(Tb,Fe)-rich oxide grain. (d) The Fe, Nd, Tb and O concentration line scan across the nodular inclusion as indicated in (c).
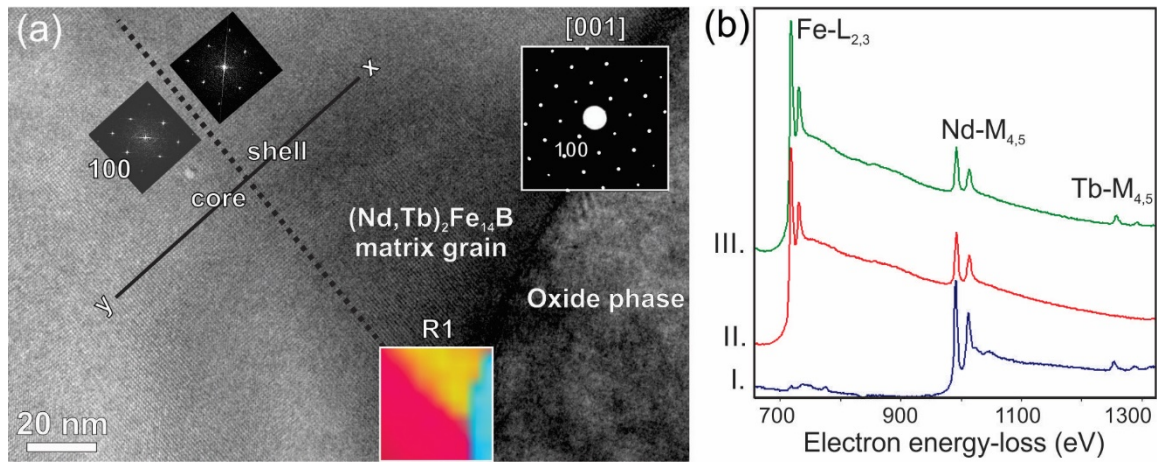


Figure 4. (a) ROI 2 showing the HRTEM image of core-shell $(Nd,Tb)_2Fe_{14}B$ matrix grain and Nd(Fe,Tb)-rich oxide phase in right image section. The inset in upper right corner is a SAED pattern acquired from the matrix grain. (b) Characteristic EELS spectra from three different specimen regions; oxide phase (I.), core (II.) and shell (III.) of the matrix grain.
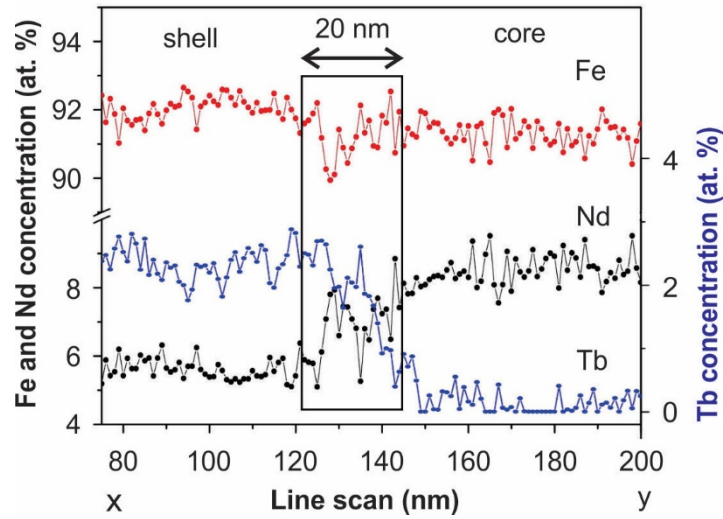
Figure 5. Nd and Tb concentration profiles obtained from line scan across the core-shell boundary (as marked in Figure 4). The transition region between the core and the shell is approximately 20 nm wide.
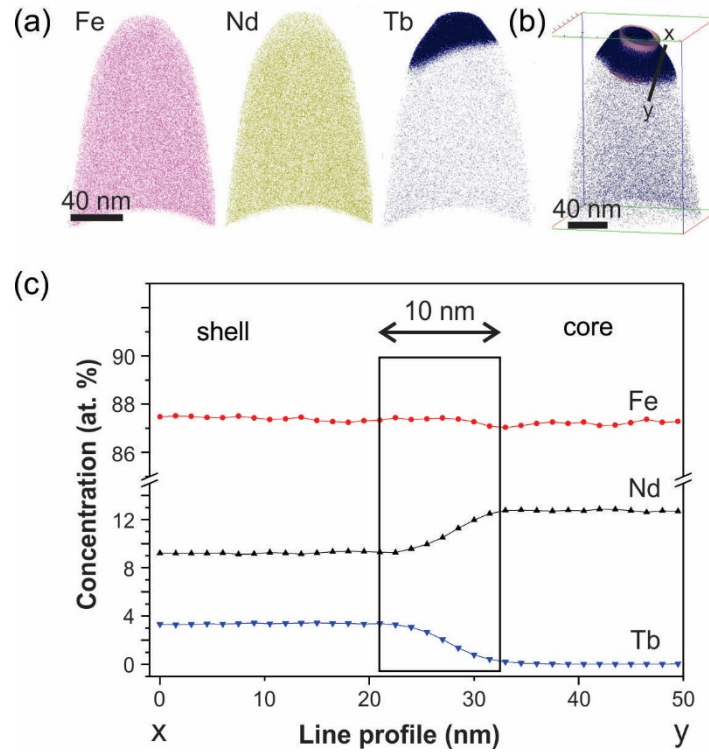


Figure 6. (a) Elemental maps Fe, Nd and Tb obtained from ROI 3. (b) 3DAP map with the indicated line profile selected perpendicular to the core-shell boundary. (c) The corresponding distribution of Nd and Tb concentration across the core-shell boundary. The transition region between the core and the shell is 10 nm wide.
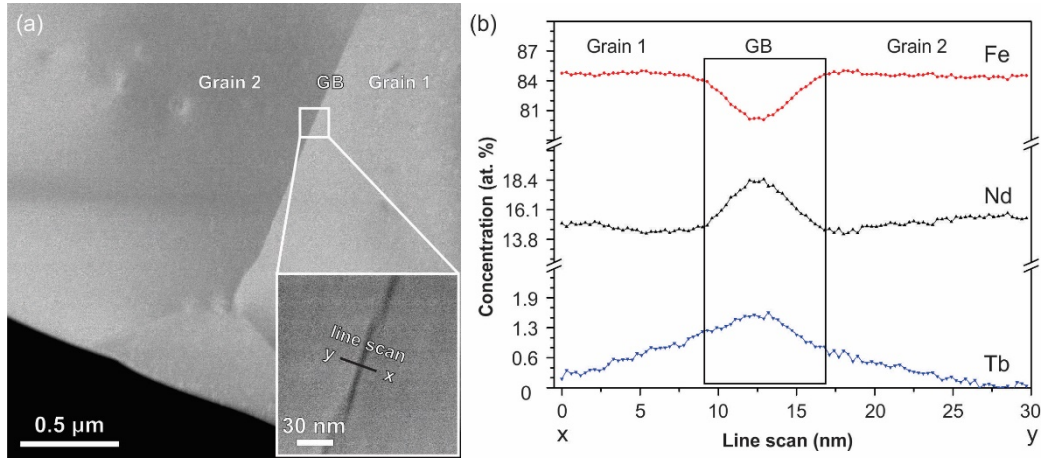
Figure 7. (a) HAADF-STEM image of GB region acquired from ROI 4. The EELS line scan is shown in the inset. (b) The Fe, Nd and Tb concentration profiles obtained from the corresponding EELS line scan.
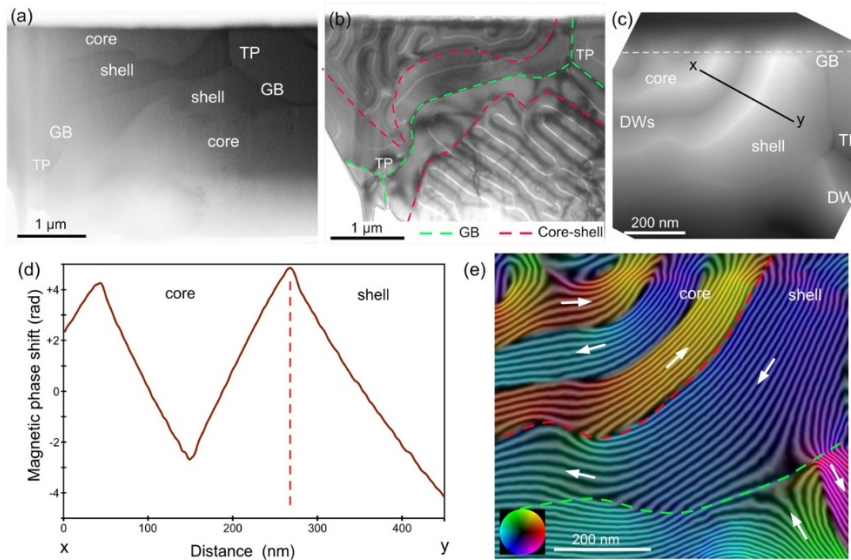


Figure 8. Magnetic microstructure of GBDP Nd-Fe-B magnet from ROI 3 with core-shell structure. (a) BF-STEM image of several grains separated with GB and TP. (b) Fresnel defocused image showing the complex network of magnetic domain walls (DWs). The defocus value used was 0.8 mm. (c) Total phase-shift map of the core-shell regions around a grain boundary region extracted from off-axis electron holography experiment. (d) Magnetic phase shift ($\phi_m$) intensity scan across three domain walls in the core-shell region marked with an arrow in (c). (e) The magnetic induction map created using the magnetic phase-shift map of the region shown in (c). The flux contour lines, colour code and arrows indicate the in-plane magnetic field strength and directions. The contour spacing is $2\pi/8 \sim 0.785$ radians.
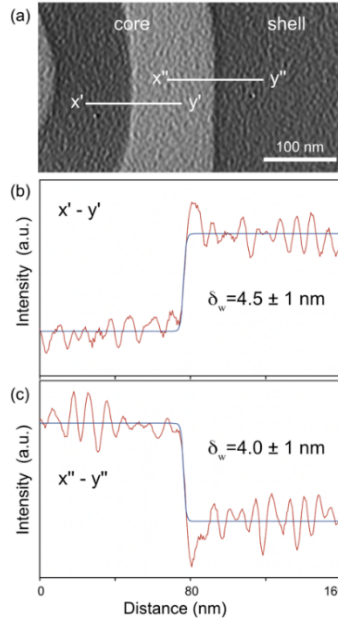
Figure 9. Domain-wall width measurements in *GBDP Nd-Fe-B* magnet from ROI 3. (a) Derivative of the phase extracted from magnetic phase shift. Intensity scans across the domain walls (b) in the core grain region and (c) at the core-shell boundary. The domain-wall widths ($\delta_w$) determined from the fit (see text).
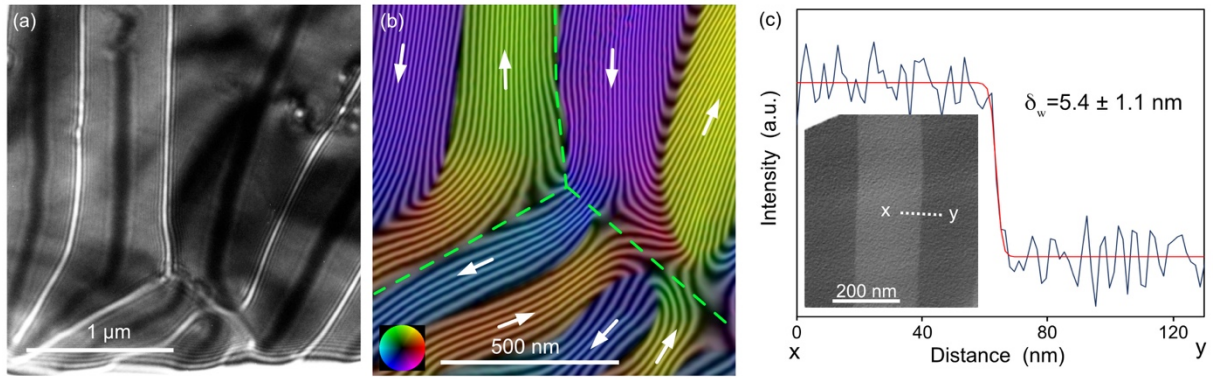


Figure 10. Magnetic microstructure of the central part (ROI 4) from *GBDP Nd-Fe-B* magnet. (a) Fresnel defocused image of the magnetic domain walls. The defocus value used was 0.8 mm. (b) Magnetic induction map of the three grains. The contour spacing is $2\pi/4 \sim 1.57$ radians. (c) Intensity distribution across the phase derivative (inset) recorded using off-axis electron holography. The $\delta_w$ is measured to be 5.4 nm $\pm 1.1$ nm.

**Supplementary material**

Supplementary Fig. 1 shows EELS spectra for (a) $Nd_2Fe_{14}B$ and (b) $Tb_2Fe_{14}B$ standards.
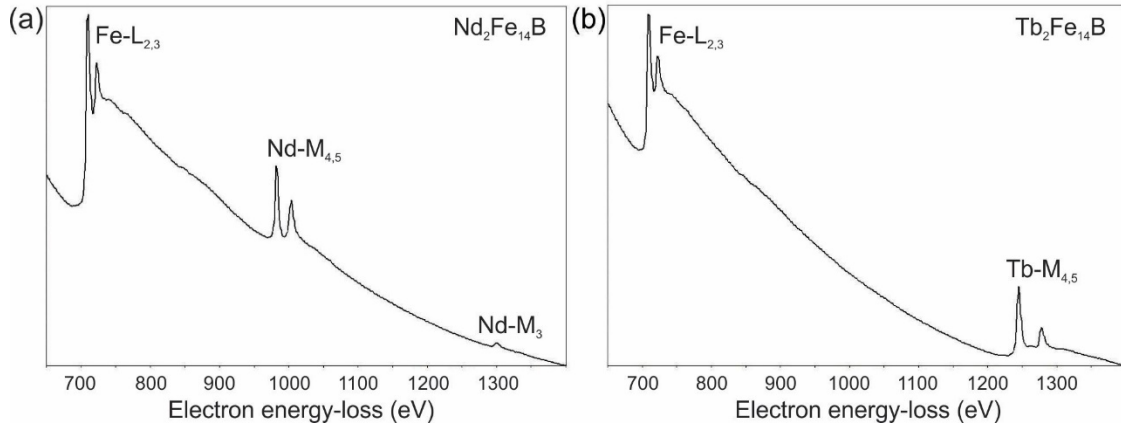


Supplementary figure 1. EELS spectra of (a) $Nd_2Fe_{14}B$ and (b) $Tb_2Fe_{14}B$ standard.

Supplementary Fig. 2 (a) shows HAADF-STEM image from the central part of *GBDP Nd-Fe B* magnet. It represents three grains separated by GB and a triple pocket. Supplementary Fig. 2 (b-d) shows compositional maps extracted from EDXS spectrum images using Fe-K, Nd-L and Tb-M signals, respectively. The concentration of the elements in each grain is homogenous, indicating that the Tb diffusion did not form a well-define shell inside the grain. The Nd/Tb enrichment and Fe depletion are observed in the triple pocket.
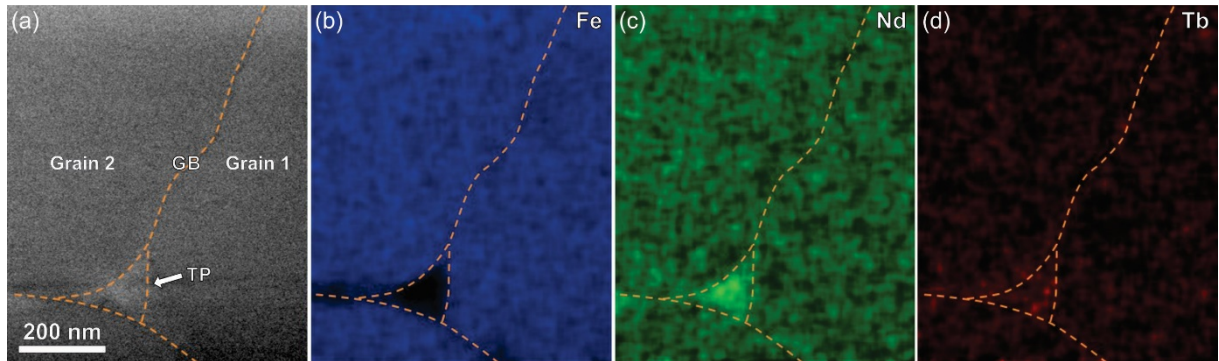


Supplementary figure 2. (a) HAADF-STEM image from the central region of *GBDP Nd-Fe-B* magnet (ROI 4). (b-d) Corresponding elemental maps extracted from EDXS spectrum imaging in STEM mode using Fe-K, Nd-L and Tb-M lines, respectively

Supplementary Fig. 3 shows a representative HAADF-STEM image with the corresponding EDXS-SI from the core-shell region for the two adjacent matrix grains separated by a grain boundary (GB) from the ROI 3. The EDXS spectrum images reveal that the Fe signal is homogeneously distributed throughout the whole analysed region. In contrast, the regions close to the GB are represented by the high Tb-M and low Nd-L signals, which indicates a Tb-rich shell, while the absence of a Tb signal and high Nd signal characterizes the core region of the matrix grain. The white dashed lines indicate the boundary between the Tb-rich shell and the Nd-Fe-B core.
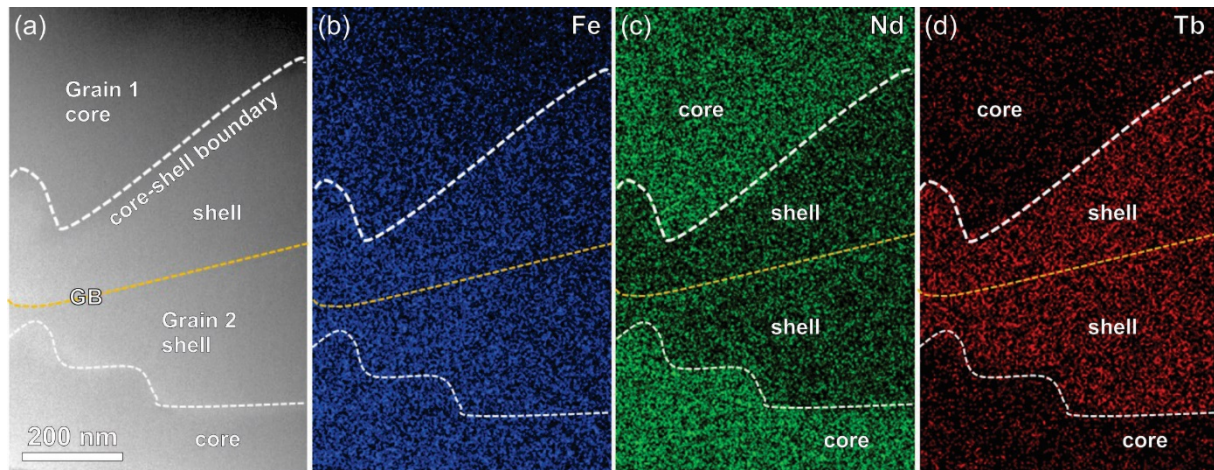
Supplementary figure 3. (a) HAADF-STEM image of core/shells at a grain boundary region extracted from ROI 3 of *GBDP Nd-Fe-B* magnet. (b-d) Corresponding elemental maps extracted from EDXS spectrum imaging in STEM mode using Fe-K, Nd-L and Tb-M lines, respectively.